nature physics

Article

https://doi.org/10.1038/s41567-024-02465-5

Topological Kerr effects in two-dimensional magnets with broken inversion symmetry

Received: 14 January 2022

Accepted: 5 March 2024

Published online: 4 April 2024

Check for updates

Xiaoyin Li[1,10], Caixing Liu[2,10], Ying Zhang[3,10], Shunhong Zhang[1], Huisheng Zhang[4], Yuchen Zhang[2,5], Wenjie Meng[2], De Hou[2], Tao Li[6], Chaoyang Kang[7], Fanyang Huang[3], Ruiguo Cao[3], Dazhi Hou[1,8], Ping Cui[1], Weifeng Zhang[7,9], Tai Min[6], Qingyou Lu[2,5], Xiaohong Xu[4], Zhigao Sheng[2] ✉, Bin Xiang[3] ✉ & Zhenyu Zhang[1] ✉

The whorls of localized moments in chiral magnetic structures, such as skyrmions, lead to a quantized topological charge, which may make them useful as next-generation information bits. So far, the most reliable way to detect the existence of skyrmions is by using the topological Hall effect, which stems from electron scattering by the emergent magnetic field manifesting the topological charge. Here we employ two-dimensional magnets to establish a magneto-optical hallmark of skyrmions, which we call the topological Kerr effect, using the recently discovered ferromagnet $CrVI_6$ as a material platform. The Kerr angle hysteresis loop of this non-centrosymmetric system exhibits two antisymmetric bumps that are absent in the centrosymmetric CrI_3 and VI_3. We develop a minimal model to further identify the bumps as direct manifestations of the topological charge, thereby providing a magneto-optical fingerprint of skyrmions with broader applicability.

The discovery of magnetic skyrmions[1,2] has triggered immense interest in topologically nontrivial magnetic structures from both scientific and technological perspectives[3–6]. These aesthetic spin textures harbour real-space geometric phases, extending the concept of topology into the field of magnetism. The topology of a given magnetic entity can be uniquely characterized by its topological charge, measuring how many times the whirling spins of the entity wrap the surface of a sphere[5]. Typically, a magnetic structure with integer topological charge can stay robust and propagate steadily, like a particle, when interacting with external probes such as electrical currents, rendering them promising information carriers for future memory and logic devices[7]. Moreover, the topological charge can manifest itself as an emergent magnetic field[8], which can affect the dynamics of electrons. In particular, for a conducting system, such a magnetic field can scatter the itinerant electrons, giving rise to the topological Hall effect (THE)[9–11], similar to the well-known anomalous Hall effect in ordinary ferromagnets[12,13]. The existence and magnitude of THE directly manifest the topological charge, making this intriguing magneto-transport phenomenon a reliable signature for detecting the presence of skyrmions[10,11,14]. As the nano-magnetism and spintronics fields rapidly develop

[1]International Center for Quantum Design of Functional Materials (ICQD), and Hefei National Laboratory, University of Science and Technology of China, Hefei, China. [2]High Magnetic Field Laboratory, HFIPS, Chinese Academy of Sciences, Hefei, China. [3]Department of Materials Science & Engineering, CAS Key Lab of Materials for Energy Conversion, Anhui Laboratory of Advanced Photon Science and Technology, University of Science and Technology of China, Hefei, China. [4]Key Laboratory of Magnetic Molecules and Magnetic Information Materials of the Ministry of Education and Research Institute of Materials Science, Shanxi Normal University, Taiyuan, China. [5]Hefei National Laboratory for Physical Sciences at the Microscale and Anhui Laboratory of Advanced Photon Science and Technology, University of Science and Technology of China, Hefei, China. [6]Center for Spintronics and Quantum Systems, State Key Laboratory for Mechanical Behavior of Materials, Department of Materials Science and Engineering, Xi'an Jiaotong University, Xi'an, China. [7]Key Laboratory for Quantum Matters and Key Laboratory of Photovoltaic Materials, Henan University, Kaifeng, China. [8]Department of Physics, University of Science and Technology of China, Hefei, China. [9]Institute of Quantum Materials and Physics, Henan Academy of Sciences, Zhengzhou, China. [10]These authors contributed equally: Xiaoyin Li, Caixing Liu, Ying Zhang. ✉e-mail: zhigaosheng@hmfl.ac.cn; binxiang@ustc.edu.cn; zhangzy@ustc.edu.cn

with ever-increasing miniaturization, the detection and characterization of skyrmions and other types of topological magnetic entities[15] become much more challenging, demanding new conceptual advances and characterization capabilities beyond the magneto-transport approaches, highly preferably in non-invasive modes.

The central accomplishment of this contribution is to deliver an important conceptual finding that is expected to have a lasting impact in skyrmionics and beyond. Specifically, we exploit the enabling power of two-dimensional (2D) magnets[16,17] to establish a magneto-optical hallmark of skyrmions, termed as the topological Kerr effect (TKE), using a newly discovered ferromagnet $CrVI_6$ as a material platform, which is valuable in its own right. The layered $CrVI_6$ compound is chemically mutated from CrI_3 (ref. 16) and VI_3 (ref. 18), but with inherent inversion symmetry breaking, thereby favouring the Dzyaloshinskii–Moriya interaction (DMI)[19,20] between the magnetic atoms, a key ingredient in stabilizing topologically nontrivial entities such as skyrmions. Strikingly, we observe two distinct antisymmetric bumps in the hysteresis loop of the Kerr rotation angle, while such bumps are absent in the parental centrosymmetric CrI_3 (ref. 16) and VI_3 (ref. 18). By modelling the spin dynamics and the magneto-optical response on a Kondo lattice with the DMI under a sweeping magnetic field, we identify the Kerr bumps as direct manifestations of the topological charge of the skyrmions, as characterized by the TKE. At a deeper level, the salient TKE originates from the skyrmion-modulated optical Hall conductivity, which can be viewed as the a.c. analogue of the THE taken in the d.c. regime. Compared with the Hall resistivity measurements, the TKE signals can be more readily extracted in a contactless mode and with sub-micrometre spatial resolution. Moreover, the tunable light frequency provides an extra degree of freedom in dealing with insulating materials, drastically expanding the applicability of the TKE beyond the THE.

The atomic structure of $CrVI_6$, as predicted via element mutation from the parental CrI_3 and VI_3 based on first-principles calculations[21,22], is illustrated in Fig. 1. This new 2D magnet is not only expected to harbour nontrivial electronic structures, but more importantly and relevantly here, its in-plane inversion symmetry is also inherently broken, enabling the system to exhibit pronounced DMI, in strong analogy to its counterpart, $CrMnI_6$ (refs. 23,24). The Dzyaloshinskii–Moriya (DM) vector points along the Cr–V bond according to Moriya's rule[25], as shown in Fig. 1. Following the predictions on its structural stability and new magnetic properties, we have synthesized bulk samples of $CrVI_6$ using the chemical vapour transport (CVT) method (Fig. 2a and Methods), with a typical high-quality flake sample of approximately 5×5 mm^2 as shown in the inset of Fig. 2b. The structure of the as-grown sample was characterized by X-ray diffraction (XRD), and the sharp XRD peaks in Fig. 2b attest to its high single crystallinity. For comparison, we have also simulated the XRD spectra using a computationally relaxed crystal structure. Given the 2D nature of the compound, only the (00l) diffraction peaks (l = 1, 2, 3, 4 and 5) can be measured. As shown in Fig. 2b, both the positions and relative intensities of the primary resonant peaks exhibit good quantitative consistency between the measured and simulated spectra, confirming that the synthesized sample adopts the layered honeycomb structure as predicted. It should also be noted that, given the honeycomb structure, the precise stoichiometry of Cr and V can be further tuned by controlling the precursor powder mixture of the CVT, and the resulting samples can be characterized by the inductively coupled plasma-atomic emission spectrometry (ICP-AES). For the specific sample shown in Fig. 2b, the mole ratio of Cr:V:I from ICP-AES is approximately 1:1.2:6 (Supplementary Table 1), slightly deviating from the perfect stoichiometry. Importantly, the mutation induced symmetry reduction and emergent DMI do not demand a rigorous 1:1 ratio of Cr:V, and the excess V content has no essential influence on our exploration of the skyrmion excitations and related magneto-optical properties. We therefore still label the samples characterized to have close Cr and V concentrations as $CrVI_6$ for simplicity and without losing generality.

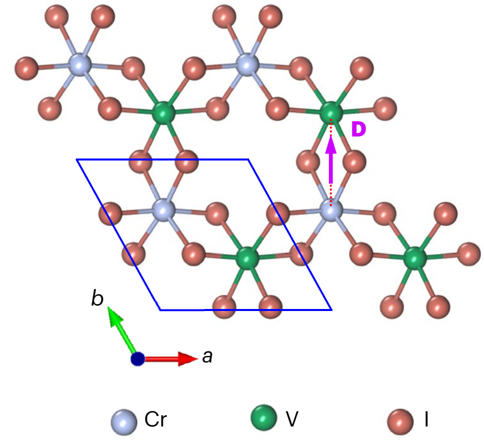

Fig. 1 | Structure and DM interaction of $CrVI_6$. Atomic structure of a $CrVI_6$ monolayer, with the blue rhombus indicating the primitive cell and **D** representing the DM vector between a nearest Cr–V pair.

To characterize the magnetic properties of bulk $CrVI_6$, we have measured the magnetization at zero-field cooling (ZFC) and field cooling (FC) respectively, by applying a magnetic field perpendicular or parallel to the sample surface to acquire the corresponding component. The curves in Fig. 2c show that the critical temperature (T_C) for the magnetic phase transition is about 51 K, while the T_C values of the parental CrI_3 and VI_3 synthesized following the same procedure are characterized to be 60 and 49 K, respectively, both consistent with previous studies[16,18]. The differences in ordering temperature and saturated magnetization between $CrVI_6$ and the two parental compounds (Supplementary Fig. 1) imply that efficient mutation has been achieved in the new 2D magnet $CrVI_6$. The M–H curves (M and H are the magnetization and external magnetic field, respectively) for the $CrVI_6$ flake are obtained through a cyclic magnetic field sweep at 10 K, and the hysteresis loops are plotted in Fig. 2d for both the in-plane and out-of-plane directions. The corresponding coercive fields are 0.10 and 0.26 T, respectively, both larger than that of CrI_3 (~0.05 T for out-of-plane coercivity)[16], indicating that $CrVI_6$ is magnetically harder. Furthermore, the magnetization saturates under a smaller field along the out-of-plane direction, which is the easy-axis of magnetization. These magnetic characteristics are all favoured for inducing and probing potential skyrmion excitations.

We now proceed to the formulation of the TKE concept based on the 2D magnet $CrVI_6$ with broken inversion symmetry and magneto-optical Kerr effect (MOKE) measurements. To ensure the surface cleanness of the samples, we have fabricated thin films from the bulk samples via mechanical exfoliation, as illustrated in Fig. 2a. Similar to CrI_3, few-layered $CrVI_6$ is air-sensitive, but encapsulation with transparent coating layers such as polymethyl methacrylate can effectively protect the thin-film samples from degradation during device fabrication and measurement. The morphology and thickness mapping shown in Fig. 2e confirm that the exfoliated $CrVI_6$ sample possesses large, flat areas with multiple thicknesses. The polar MOKE measurements were carried out on a selected flat area of a fixed thickness (Methods), as illustrated in Fig. 3a,b. The incident light and sweeping magnetic field are both perpendicular to the sample surface, and the field-dependent Kerr rotation angle θ_K is recorded. In Fig. 3b, we also show the optical image of an ~80-nm-thick $CrVI_6$ film on the SiO_2 substrate, with the corresponding temperature-dependent hysteresis loops of the Kerr rotation angle summarized in Fig. 3c. Overall, the loops share similar shape and temperature dependence with the bulk M–H curves, showing that the $CrVI_6$ film remains ferromagnetic (FM) when exfoliated from the bulk, but the remanent θ_K disappears at ~36 K, indicating that the FM ordering temperature

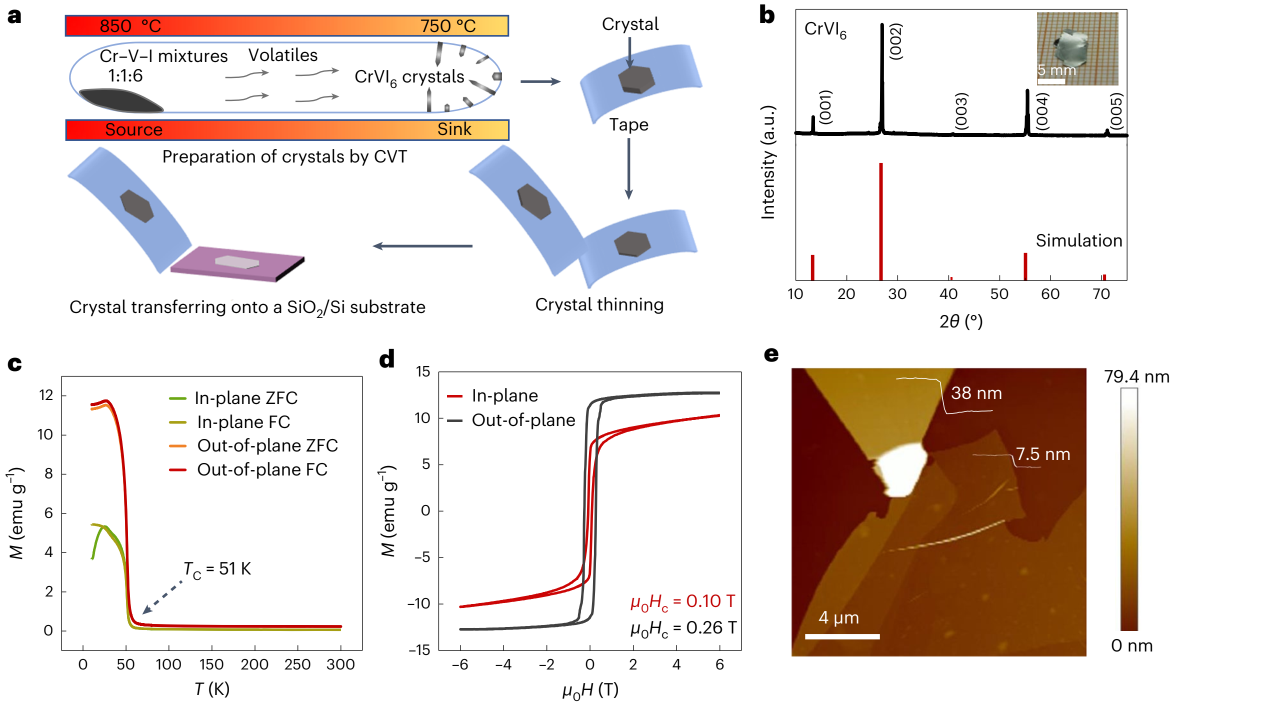

Fig. 2 | Preparation and characterization of bulk and thin-film samples of $CrVI_6$. **a**, Schematic protocols for the sample preparation by CVT and exfoliation by taping. **b**, Experimental (black) and simulated (red) XRD patterns of the cleaved $CrVI_6$ crystal. Inset: optical image of a typical $CrVI_6$ flake used for the XRD measurement. **c**, In-plane and out-of-plane magnetizations of a $CrVI_6$ flake at ZFC and FC, respectively. For FC, the cooling field is applied parallel to the magnetization measurement direction. emu, electromagnetic unit, which is the unit of magnetic moment (1 emu = 1 erg G^{-1}). **d**, Magnetization hysteresis loops of a $CrVI_6$ flake measured at 10 K. **e**, Atomic-force-microscopy morphology of the exfoliated few-layer $CrVI_6$ on the SiO_2/Si substrate. The colour bar on the right maps the thickness variations of the sample.

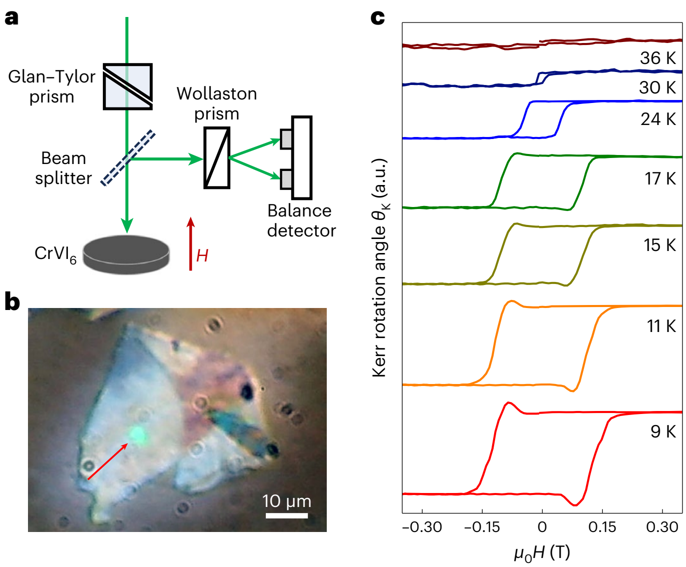

Fig. 3 | Magneto-optical Kerr effect measurements and TKE in $CrVI_6$. **a**, Optical path for polar MOKE measurements. **b**, Optical image of an exfoliated $CrVI_6$ thin film on the SiO_2/Si substrate, with the sample thickness of ~80 nm. The green spot indicated by the red arrow identifies the region where the MOKE data were taken. **c**, Temperature-dependent hysteresis loops of the Kerr rotation angle, with the bumps signifying the presence of the TKE.

is lowered from that of the bulk, as expected. The hysteresis loops of the Kerr angle exhibit two antisymmetric bumps in the vicinity of magnetization reversal, constituting an important experimental finding in a 2D magnet.

To gain more insight into the underlying physical origin of the bump features in the hysteresis loop of the Kerr angle, we make the following observations. First, the bumps modulate the Kerr angle hysteresis loop in a manner closely resembling the THE in magneto-transport measurements of skyrmionic systems. Given that pronounced DMI is present in $CrVI_6$ due to inversion symmetry breaking, it is natural to conjecture that skyrmionic excitations will also emerge in the system, and the bump features are microscopically rooted in the topological charges of the skyrmionic excitations as well. Indeed, our low-temperature magnetic force microscope (MFM) imaging (Methods) on the surface of a bulk $CrVI_6$ sample reveals distinct real-space magnetic structures, which evolve from striped to circular shapes upon applying an out-of-plane magnetic field (Supplementary Fig. 2 and Note 1). Such evolution behaviours are strong indications of skyrmion formation, as widely seen in real-space imaging[26] and magnetics simulations (ref. 27 and Supplementary Fig. 3 for the present system). In particular, the coincidence of the field range for the coexistence of topological magnetic structures in both striped and circular shapes and for the MOKE bumps points to the excitation of skyrmions with the assistance of the external magnetic field. It should also be noted that the observed topological magnetic entities are much larger in lateral size for the bulk samples, but are expected to substantially shrink their sizes for thin-film samples[28,29], an important aspect to be directly validated in future experimental studies. Second, the bump features only survive below a critical temperature of $T_M \approx 17$ K (here we use the label 'M' to imply its metastable nature), lower than the ferromagnetic ordering temperature of the film sample ($T_C \approx 36$ K), again implying the existence and metastable nature of the skyrmions in the present system and consistent with the relative stabilities of these two magnetic orderings[1,30,31]. Third, we have confirmed that the bump features are robust, as seen consistently using 20 different $CrVI_6$ samples with the thickness varying from

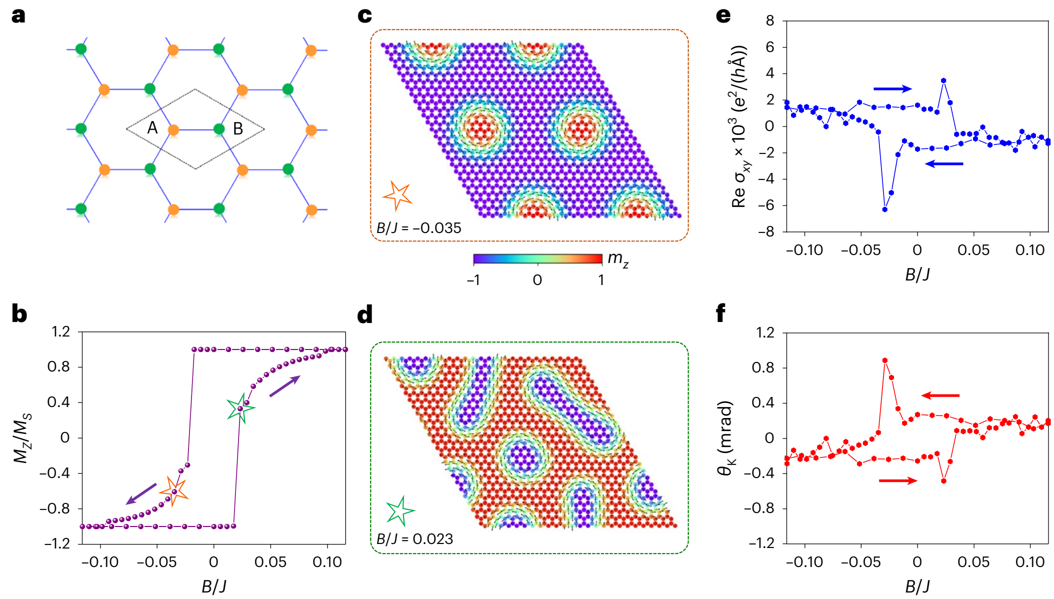

Fig. 4 | Simulated magneto-optical responses and TKE on a $CrVI_6$ lattice with DMI. a, The honeycomb geometry of the Kondo lattice modelling a $CrVI_6$ monolayer, with two different magnetic species labelled by A and B and containing two different spin moments. **b**, Hysteresis loop of the magnetization (out-of-plane component, normalized by the saturation value) of the 2D spin lattice, simulated using a 25 × 25 supercell containing 1,250 sites. The arrows denote the field sweeping directions. **c**,**d**, Snapshots of the equilibrium spin configurations under the selected magnetic fields as indicated by the orange and green stars in **b**, displaying the emergence of the skyrmionic excitations (including severely distorted/elongated ones). In both **c** and **d**, the arrows and colours map the in-plane and out-of-plane spin components, respectively. **e**, Evolution of the real part of the optical Hall conductivity in units of $e^2/(h\text{Å})$, taken along the same hysteresis loop shown in **b**, with e, h and Å the elementary charge, Planck constant and angstrom, respectively. **f**, Corresponding hysteresis loop of the Kerr rotation angle, displaying the TKE as experimentally observed. The light frequency in **e** and **f** is set to $\hbar\omega$ = 2.3 eV, comparable to the photon energy for MOKE measurements (2.33 eV).

70 to 120 nm (Supplementary Fig. 4), pointing to the intrinsic property nature of the newly identified 2D magnet.

Going beyond the above conjecture, we now develop a minimal model to further solidify the claim that the bump features are inherently also tied to the topological charge of the skyrmions, but representing the magneto-optical signature. We first note that some recent studies have shown indications of the skyrmions in the corresponding resonant optical Hall conductivity measurements, with the skyrmions constructed a priori[32,33]. In our study, the central ingredient is the presence of the DMI, as rightfully justified by the in-plane inversion symmetry breaking of the $CrVI_6$ system. The coupling between the electrons and localized moments is encoded on a Kondo lattice[34] with a honeycomb geometry as shown in Fig. 4a, wherein the bipartite asymmetry faithfully captures the non-centrosymmetric feature of the $CrVI_6$ system. Each site is populated with a single electronic orbital plus a localized spin, with the former manifesting the electrical and optical properties, while the latter registering the magnetic moments of the Cr/V atoms. A tight-binding Hamiltonian, describing the electron scattering by the localized moments, reads:

$$H = t\sum_{<i,j>} c_i^\dagger c_j + \mathrm{i}\lambda_{\mathrm{SO}} \sum_{<i,j>,\alpha\beta} c_{i\alpha}^\dagger \left(\boldsymbol{\sigma}\cdot\hat{\mathbf{d}}_{ij}\right)_{\alpha\beta} c_{j\beta} + \lambda_V \sum_i \tau_i c_i^\dagger c_i + \sum_{i,\alpha\beta} \lambda_{M,i} c_{i\alpha}^\dagger (\mathbf{m}_i\cdot\boldsymbol{\sigma})_{\alpha\beta} c_{i\beta}. \quad (1)$$

Here $c_{i\alpha}^\dagger$ ($c_{j\beta}$) is the fermionic creation (annihilation) operator, with the subscripts i and j indexing the orbital degrees of freedom, and α and β indexing the spin degrees. The first term represents hopping between two nearest sites, and the second term takes the form of the Weyl-type spin-orbit coupling[35,36] that conforms to the symmetry of the system (Supplementary Note 2). The unit vector $\hat{\mathbf{d}}_{ij}$ points from site i to j, and $\boldsymbol{\sigma} = (\sigma_x, \sigma_y, \sigma_z)$ is the Pauli vector. The third term describes the on-site energy, where τ_i = +1 or −1 indicates the A or B sublattice, respectively, and λ_v represents the on-site energy difference of the two sublattices. The last term describes the on-site Hund's coupling between itinerant electrons and localized magnetic moments at site i, $\mathbf{m}_i$, and the coupling strength $\lambda_{M,i}$ (M = A, B) also has a sublattice dependence. The exchange couplings of the magnetic lattice {$\mathbf{m}_i$} are described by a Heisenberg spin Hamiltonian as

$$H_M = -J\sum_{<i,j>} \mathbf{n}_i\cdot\mathbf{n}_j - \sum_{<i,j>} \mathbf{D}_{ij}\cdot(\mathbf{n}_i\times\mathbf{n}_j) - \sum_i A_{iz} n_{iz}^2 - \mu_i \sum_i \mathbf{B}\cdot\mathbf{n}_i. \quad (2)$$

Here, the first and second terms represent the isotropic Heisenberg exchange coupling and the chiral DMI between two nearest localized spins, respectively. The third term is the single-ion anisotropy energy, which is contributed solely by the z component of the moments due to the D_3 symmetry of the material[37]. The last term is the Zeeman energy, with **B** the external magnetic field multiplied by the Bohr magneton and expressed in units of joules. The normalized spin $\mathbf{n}_i$ satisfies $\mathbf{m}_i = \mu_i\mathbf{n}_i$ (we set $\mu_{\mathrm{Cr}} = 3\,\mu_{\mathrm{B}}$ and $\mu_{\mathrm{V}} = 2\,\mu_{\mathrm{B}}$ for the Cr and V sites, respectively).

The magnetization dynamics of the spin lattice under cyclic magnetic field sweeping is simulated by numerically integrating the Landau–Lifshitz–Gilbert equation[38,39] (Methods), with the equilibrium configurations at each field analysed. In our simulations, we set a positive J favouring ferromagnetic coupling, $A_{iz} = 0.02J$ and $|\mathbf{D}_{ij}| = 0.5J$, with the DM vector pointing from site i to j. The out-of-plane magnetization is plotted in Fig. 4b, forming a hysteresis loop featured by retarded saturation when **B** exceeds the coercive field, a pronounced signature for the emergence of chiral magnetic structures[40,41]. Figure 4c,d displays the snapshot spin configurations at the fields near the magnetization reversal, where we directly observe collectively excited skyrmions in the out-of-plane FM background. Taking the field descending branch as an example, when the overall magnetization is reversed from +z to −z by the applied magnetic field, multiple domains with opposite magnetizations are formed in the system, separated by Bloch domain walls, as imposed by the symmetry of the Bloch-type DMI. Upon field descending, domains magnetized along $+z$ are gradually eroded by those with $-z$ magnetization. In particular, the shrinkage of the domains coincides with the birth of the skyrmions (or skyrmion bubbles with distorted or elongated geometry). By tracking the topological charge within the supercell (Supplementary Fig. 5), we can detect skyrmionic excitations within a proper range of the **B** field, and such excitations are annihilated and merged into the FM background when the **B** exceeds a critical value. Here, the relatively large $|\mathbf{D}_{ij}|/J$ ratio of 0.5 is a technical treatment for saving computational cost, because it would enable formation of smaller-sized skyrmions and allow simulation of the TKE within a moderate supercell in subsequent tight-binding calculations. As a crosscheck, we have also demonstrated in a large 100 × 100 supercell containing 20,000 sites that a more realistic $|\mathbf{D}_{ij}|/J$ ratio of 0.2 can give rise to similar hysteresis loops as well, albeit with a more complicated evolution of topological charge (Supplementary Fig. 6).

With the magnetic configurations in hand, we now can quantify the magneto-optical response by inserting the snapshot spin configurations $\{\mathbf{m}_i(\mathbf{B})\}$ into equation (1) to calculate the optical conductivity tensor $\boldsymbol{\sigma}(\omega)$ (ref. 42) (Methods). The adiabatic approximation is made here, because the depinning effect of skyrmions by the optical Hall current should be minor, as estimated within the context of THE in typical transport measurements[43,44]. The tight-binding Hamiltonian is parametrized (in electron volts) with $t = 0.4$, $\lambda_{SO} = 0.02$, $\lambda_V = 0.02$, $\lambda_A = 0.40$ and $\lambda_B = 0.70$, which collectively produce a band splitting with an energy scale comparable to the photon energy of the laser for MOKE measurements. In Fig. 4e, we plot the real antisymmetric part of the off-diagonal component of the optical conductivity $\sigma_{xy}(\omega)$ as a function of applied magnetic field. One can see qualitatively similar and pronounced bump features in essentially the same field range where the skyrmionic excitations emerge. Recalling that in the d.c. limit, the σ_{xy} hysteresis loop of a skyrmion-hosting material also exhibits bump signals known as the THE, the loop in Fig. 4e can be viewed as the analogue of the THE in the high-frequency a.c. regime, which itself is intriguing and can be potentially detected via optical reflectivity and transmission measurements[45].

To compare directly with the results of the MOKE measurements, we go one step further, by substituting the optical conductivity $\boldsymbol{\sigma}(\omega)$ into the complex polar Kerr angle defined by[46,47]

$$\theta_K + i\eta_K = \frac{2Z_0 d\sigma_{xy}}{1 - (n_s + Z_0 d\sigma_{xx})^2}. \quad (3)$$

Here, the real part θ_K represents the rotation angle between the major axis of the reflected light and polarization direction of the incident light, while the imaginary part η_K quantifies the ellipticity of the reflected light (Supplementary Fig. 7). This equation can be derived by counting the difference of reflection coefficients of the right and left circularly polarized light and is valid under conditions that the complex Kerr angle $(\theta_K + i\eta_K)$ is small and $\sigma_{xy} \ll \sigma_{xx}$. Here $Z_0 = 376.730\ \Omega$ is the impedance of free space, and n_s is the refractive index of the substrate, taken to be 1.5 for SiO_2; σ_{xx} and σ_{xy} are the longitudinal and transverse components of the optical conductivity, with the latter exemplified in Fig. 4e. By taking $d = 7$ Å as the thickness of a $CrVI_6$ monolayer, we finally obtain the θ_K hysteresis loop as shown in Fig. 4f. The results qualitatively reproduce the experimentally identified TKE in $CrVI_6$ thin films, as signified by the bump features near the coercive fields. Our simulations have further confirmed that the TKE characteristic is robust against varying the light frequency (Supplementary Figs. 8–10). The range of the **B** field for the onset of the θ_K bumps and emergence of the skyrmions also coincide with each other, convincingly demonstrating the topological origin of such magneto-optical responses. The skyrmions have a pronounced contribution to θ_K, with the sign opposite to the component from the corresponding FM background (see examples in Supplementary Fig. 11, where the skyrmion cores point to $-z$ while the FM background is along $+z$) and the magnitude varying with the skyrmion size (Supplementary Fig. 12), which collectively dictate the shape of the bumps (Supplementary Note 3). As a comparative study, we have also examined the hysteresis loop of the Kerr rotation angle for a model pristine CrI_3 system without the DMI, confirming the absence of bump feature (Supplementary Fig. 13).

Before closing, we discuss the broader perspectives of the TKE, including its connections with important related developments. First, its physical origin is convincingly attributed to the topological charges encoded in the skyrmions. In this regard, the spin chirality in magnetic systems with non-collinear alignments has been shown to possess pronounced magneto-optical response[48–50]. Since such chiral spin structures may also be accompanied by topological charges, it should be highly desirable to explore whether the TKE is also present and observable in those materials with non-collinear long-range magnetic orders under a proper magnetic field. Second, although the TKE concept is developed using the newly discovered non-centrosymmetric 2D magnet of $CrVI_6$, it is expected to be broadly applicable to many other systems, where bump features have been reported but the precise physical origin remains to be definitely identified[51,52]. Third, the tunable frequency of the probing light makes TKE inherently more advantageous for detection of skyrmions in insulating systems, which complements and goes beyond the THE, especially for miniaturized systems where electrical contacts become very demanding. Fourth, with the establishment of the TKE concept, the bump features in the Kerr rotation angle can serve as a new and reliable signature in characterizing the existence of the skyrmions and potentially other topological entities, especially when real-space imaging techniques are practically not accessible (for example, at too-low temperatures). Finally, we expect more observations of TKE by revisiting magnetic systems whose skyrmionic phases have already been characterized by complementary techniques such as real-space imaging.

In summary, using $CrVI_6$ as an enabling platform of a 2D magnet, we have established the TKE as a fundamentally intriguing and technically important magneto-optical response of skyrmions and other topologically nontrivial magnetic entities. The TKE is signified by the emergence of two antisymmetric bumps in the Kerr angle hysteresis loop, and the underlying physical origin is tied to the broken in-plane inversion symmetry and resultant DMI, a crucial ingredient for the existence of the skyrmions. Given its non-invasive nature of probing, the TKE provides an alternative fingerprint to probe skyrmions in chiral magnets, with broader applicability beyond the THE, especially for insulating systems. In addition to providing a fertile platform for the formulation of the TKE, the realization of $CrVI_6$ with designer inversion symmetry breaking and resultant strong DMI also exemplifies a powerful way to discover new 2D magnets via element mutation.

Note added in proof: After the initial submission, we discovered the appearance of a very recent work[53] reporting MOKE signature in a previously established skyrmion-hosting material of Gd_2PdSi_3 (ref. 11). In essence, this work[53] not only provides an independent and complementary support to the central claim of the present work connecting skyrmions with MOKE anomalies, but also effectively expands the applicability of TKE from nonmetallic to metallic systems.

Online content

Any methods, additional references, Nature Portfolio reporting summaries, source data, extended data, supplementary information, acknowledgements, peer review information; details of author contributions and competing interests; and statements of data and code availability are available at https://doi.org/10.1038/s41567-024-02465-5.

References

1. Mühlbauer, S. et al. Skyrmion lattice in a chiral magnet. *Science* **323**, 915–919 (2009).
2. Yu, X. Z. et al. Real-space observation of a two-dimensional skyrmion crystal. *Nature* **465**, 901–904 (2010).

3. Nagaosa, N. & Tokura, Y. Topological properties and dynamics of magnetic skyrmions. *Nat. Nanotechnol.* **8**, 899–911 (2013).
4. Göbel, B., Mertig, I. & Tretiakov, O. A. Beyond skyrmions: review and perspectives of alternative magnetic quasiparticles. *Phys. Rep.* **895**, 1–28 (2021).
5. Tokura, Y. & Kanazawa, N. Magnetic skyrmion materials. *Chem. Rev.* **121**, 2857 (2021).
6. Back, C. et al. The 2020 skyrmionics roadmap. *J. Phys. D: Appl. Phys.* **53**, 363001 (2020).
7. Fert, A., Cros, V. & Sampaio, J. Skyrmions on the track. *Nat. Nanotechnol.* **8**, 152–156 (2013).
8. Taguchi, Y., Oohara, Y., Yoshizawa, H., Nagaosa, N. & Tokura, Y. Spin chirality, Berry phase, and anomalous Hall effect in a frustrated ferromagnet. *Science* **291**, 2573–2576 (2001).
9. Bruno, P., Dugaev, V. K. & Taillefumier, M. Topological Hall effect and Berry phase in magnetic nanostructures. *Phys. Rev. Lett.* **93**, 096806 (2004).
10. Neubauer, A. et al. Topological Hall effect in the A phase of MnSi. *Phys. Rev. Lett.* **102**, 186602 (2009).
11. Kurumaji, T. et al. Skyrmion lattice with a giant topological Hall effect in a frustrated triangular-lattice magnet. *Science* **365**, 914–918 (2019).
12. Nagaosa, N., Sinova, J., Onoda, S., MacDonald, A. H. & Ong, N. P. Anomalous Hall effect. *Rev. Mod. Phys.* **82**, 1539–1592 (2010).
13. Xiao, D., Chang, M.-C. & Niu, Q. Berry phase effects on electronic properties. *Rev. Mod. Phys.* **82**, 1959–2007 (2010).
14. Huang, S. X. & Chien, C. L. Extended skyrmion phase in epitaxial FeGe(111) thin films. *Phys. Rev. Lett.* **108**, 267201 (2012).
15. Nayak, A. K. et al. Magnetic antiskyrmions above room temperature in tetragonal Heusler materials. *Nature* **548**, 561–566 (2017).
16. Huang, B. et al. Layer-dependent ferromagnetism in a van der Waals crystal down to the monolayer limit. *Nature* **546**, 270–273 (2017).
17. Gong, C. et al. Discovery of intrinsic ferromagnetism in two-dimensional van der Waals crystals. *Nature* **546**, 265–269 (2017).
18. Tian, S. et al. Ferromagnetic van der Waals crystal VI_3. *J. Am. Chem. Soc.* **141**, 5326–5333 (2019).
19. Dzyaloshinsky, I. A thermodynamic theory of "weak" ferromagnetism of antiferromagnetics. *J. Phys. Chem. Solids* **4**, 241–255 (1958).
20. Moriya, T. Anisotropic superexchange interaction and weak ferromagnetism. *Phys. Rev.* **120**, 91–98 (1960).
21. Zhang H., Cui P., Xu X. & Zhang Z. A family tree of two-dimensional magnetic materials with tunable topological properties. Preprint at https://doi.org/10.48550/arXiv.2112.10924 (2021).
22. Fayazi Y., Jacobsson L. & Gustafsson F. *First Principles Studies of 2D Magnets*. BSc thesis, Uppasala Univ. (2022).
23. Zhang, H., Yang, W., Cui, P., Xu, X. & Zhang, Z. Prediction of monolayered ferromagnetic $CrMnI_6$ as an intrinsic high-temperature quantum anomalous Hall system. *Phys. Rev. B* **102**, 115413 (2020).
24. Zhang, S. et al. Giant Dzyaloshinskii–Moriya interaction, strong XXZ-type biquadratic coupling, and bimeronic excitations in the two-dimensional $CrMnI_6$ magnet. *npj Quantum Mater* **8**, 38 (2023).
25. Moriya, T. New mechanism of anisotropic superexchange interaction. *Phys. Rev. Lett.* **4**, 228–230 (1960).
26. Powalla, L. et al. Seeding and emergence of composite skyrmions in a van der Waals magnet. *Adv. Mater.* **35**, 2208930 (2023).
27. Wang, X. R., Hu, X.-C. & Sun, Z.-Z. Topological equivalence of stripy states and skyrmion crystals. *Nano Lett.* **23**, 3954–3962 (2023).
28. Wang, H. et al. Characteristics and temperature-field-thickness evolutions of magnetic domain structures in van der Waals magnet Fe_3GeTe_2 nanolayers. *Appl. Phys. Lett.* **116**, 192403 (2020).
29. Lu, E. et al. Analytic theory for Néel skyrmion size, accounting for finite film thickness. *J. Magn. Magn. Mater.* **584**, 171044 (2023).
30. Adams, T. et al. Long-wavelength helimagnetic order and skyrmion lattice phase in Cu_2OSeO_3. *Phys. Rev. Lett.* **108**, 237204 (2012).
31. Yu, X. Z. et al. Near room-temperature formation of a skyrmion crystal in thin-films of the helimagnet FeGe. *Nat. Mater.* **10**, 106–109 (2011).
32. Bhowmick, T. K., De, A. & Lake, R. K. High figure of merit magneto-optics from interfacial skyrmions on topological insulators. *Phys. Rev. B* **98**, 024424 (2018).
33. Sorn, S., Yang, L. & Paramekanti, A. Resonant optical topological Hall conductivity from skyrmions. *Phys. Rev. B* **104**, 134419 (2021).
34. Martin, I. & Batista, C. D. Itinerant electron-driven chiral magnetic ordering and spontaneous quantum Hall effect in triangular lattice models. *Phys. Rev. Lett.* **101**, 156402 (2008).
35. Mera Acosta, C., Yuan, L., Dalpian, G. M. & Zunger, A. Different shapes of spin textures as a journey through the Brillouin zone. *Phys. Rev. B* **104**, 104408 (2021).
36. Weyl, H. Elektron und Gravitation. I. *Z. Physik* **56**, 330–352 (1929).
37. Šabani, D., Bacaksiz, C. & Milošević, M. V. Ab initio methodology for magnetic exchange parameters: generic four-state energy mapping onto a Heisenberg spin Hamiltonian. *Phys. Rev. B* **102**, 014457 (2020).
38. Gilbert, T. L. A phenomenological theory of damping in ferromagnetic materials. *IEEE Trans. Magn.* **40**, 3443–3449 (2004).
39. Müller, G. P. et al. Spirit: multifunctional framework for atomistic spin simulations. *Phys. Rev. B* **99**, 224414 (2019).
40. Legrand, W. et al. Room-temperature stabilization of antiferromagnetic skyrmions in synthetic antiferromagnets. *Nat. Mater.* **19**, 34–42 (2020).
41. Park, T.-E. et al. Néel-type skyrmions and their current-induced motion in van der Waals ferromagnet-based heterostructures. *Phys. Rev. B* **103**, 104410 (2021).
42. Sivadas, N., Okamoto, S. & Xiao, D. Gate-controllable magneto-optic Kerr effect in layered collinear antiferromagnets. *Phys. Rev. Lett.* **117**, 267203 (2016).
43. Schulz, T. et al. Emergent electrodynamics of skyrmions in a chiral magnet. *Nat. Phys.* **8**, 301–304 (2012).
44. Xiao, J., Zangwill, A. & Stiles, M. D. Spin-transfer torque for continuously variable magnetization. *Phys. Rev. B* **73**, 054428 (2006).
45. Mak, K. F. et al. Measurement of the optical conductivity of graphene. *Phys. Rev. Lett.* **101**, 196405 (2008).
46. Kim, M. H. et al. Determination of the infrared complex magnetoconductivity tensor in itinerant ferromagnets from Faraday and Kerr measurements. *Phys. Rev. B* **75**, 214416 (2007).
47. Valdés Aguilar, R. et al. Terahertz response and colossal Kerr rotation from the surface states of the topological insulator Bi_2Se_3. *Phys. Rev. Lett.* **108**, 087403 (2012).
48. Feng, W., Guo, G.-Y., Zhou, J., Yao, Y. & Niu, Q. Large magneto-optical Kerr effect in noncollinear antiferromagnets Mn_3X (X = Rh, Ir, Pt). *Phys. Rev. B* **92**, 144426 (2015).
49. Feng, W. et al. Topological magneto-optical effects and their quantization in noncoplanar antiferromagnets. *Nat. Commun.* **11**, 118 (2020).

https://doi.org/10.1038/s41567-024-02465-5

50. Higo, T. et al. Large magneto-optical Kerr effect and imaging of magnetic octupole domains in an antiferromagnetic metal. *Nat. Photon.* **12**, 73–78 (2018).
51. Liu, J., Singh, A., Kuerbanjiang, B., Barnes, C. H. W. & Hesjedal, T. Kerr effect anomaly in magnetic topological insulator superlattices. *Nanotechnology* **31**, 434001 (2020).
52. Bartram, F. M. et al. Anomalous Kerr effect in $SrRuO_3$ thin films. *Phys. Rev. B* **102**, 140408 (2020).
53. Kato, Y. D., Okamura, Y., Hirschberger, M., Tokura, Y. & Takahashi, Y. Topological magneto-optical effect from skyrmion lattice. *Nat. Commun.* **14**, 5416 (2023).

Methods

Materials fabrication and characterization

Bulk samples of $CrVI_6$ were synthesized by a CVT method. The chromium powder (99.99%, Aladdin), vanadium powder (99.99%, Aladdin) and anhydrous iodine beads (99.99%, Aladdin) were homogeneously mixed with a ratio of 1:1:6 and then loaded in a quartz tube (13 mm inner diameter, 15 mm outer diameter and 150 mm in length). The quartz tube was vacuumed, then sealed and placed into a tube furnace (Fig. 2a). The high and low temperatures of the double-temperature zone furnace were set to 850 and 750 °C, respectively. It took 3,000 min to heat the furnace from room temperature to target temperatures. Then the temperatures were maintained at the set point for seven days before cooling down to room temperature. Afterwards, a single crystal $CrVI_6$ was observed in the sealed quartz tube. The structure and magnetic properties were characterized via room-temperature XRD and via a superconducting quantum interference device, respectively. ICP-AES was utilized to precisely quantify the chemical content of the samples.

Few-layered $CrVI_6$ was prepared by a mechanical exfoliation method from the bulk single crystal by Scotch Tape following the recipe illustrated in Fig. 2a of the main text. After exfoliation, the few-layer sample of $CrVI_6$ was transferred from the Scotch Tape to a 300-nm-thick SiO_2/Si substrate, which provides good optical contrast for $CrVI_6$ with different thickness. The entire set of processes—few-layer sample preparation, thickness measurements and morphology imaging (by atomic force microscopy)—were carried out in a glovebox with extremely low H_2O and O_2 levels (≤0.1 ppm).

MOKE measurements

The $CrVI_6$ flakes were covered by ~1-μm-thick polymethyl methacrylate to prevent them from reacting with oxygen and moisture. Encapsulated $CrVI_6$ flakes then were transferred from the Argon-protection glovebox to a low-vibration and high-vacuum optical cryostat (CS204SF-FMX-20, Advanced Research Systems) for further MOKE experiments. The time for the entire transfer process did not exceed 15 s.

Polar MOKE measurements were performed using a standard laboratory-made MOKE setup. The temperature range of the setup is 9–300 K, and the magnetic field range is 0–0.65 T. As shown in Fig. 3a, both the magnetic field and the laser light were applied perpendicular to the sample surface. The laser of 532 nm wavelength with the power of 9 μW was polarized by a Glan prism and focused on the sample through a ×50 objective lens. The reflected probe beam from the sample surface was sent to the Wollaston polarizer to detect the output signal voltage using two Si photo-diodes. The difference between two output signal voltages, divided by their sum, is used to determine the Kerr rotation angle. An SR865 lock-in amplifier and a chopper were used to improve the signal-to-noise ratio of the Kerr signal. Through iterative exfoliation, we are able to reduce the film thickness to ~6.6 nm. Thin films with thickness of tens of nanometres, with the most pronounced magneto-optical response, were used for MOKE measurements, the base by which the TKE is established. The laser spot size for the MOKE measurements is ~2 μm, which should be adequate to cover multiple skyrmions, typically in size of hundreds of nanometres, as seen in other van der Waals magnetic thin films of similar thickness[26].

Real-space imaging of magnetic structures in a custom-designed MFM system

A quartz tube containing the $CrVI_6$ samples was transferred to an argon-filled glovebox (H_2O ≤ 0.01 ppm, O_2 ≤ 0.01 ppm) to protect the sample from potential water and oxygen contamination. The quartz tube was then opened within the glovebox, and an appropriate size of $CrVI_6$ was selected for subsequent MFM characterization. The MFM experiments were carried out using a custom-designed temperature-variable MFM system, which was equipped with a 12 T superconducting magnet sourced from Oxford Instruments. The target $CrVI_6$ sample was positioned on a blue tape to enable exfoliation of a clean and flat surface. Subsequently, the $CrVI_6$ sample was securely affixed within the MFM mirror body (sample holder). A piezoresistive cantilever (PRC400, Hitachi High-Tech Science Corporation) with a pyramid-shaped tip was employed as the force sensor. The cantilever was meticulously adjusted to position the tip directly above the sample. Finally, the mirror body was hermetically sealed within an argon-filled enclosure and transferred to the Oxford superconducting magnet for MFM characterization. By implementing these procedures, the $CrVI_6$ samples were effectively prevented from exposure to the air throughout the process of MFM characterization.

The MFM images were collected in constant height mode, with the tip lifted to a height of ~150 nm from the sample surface. For each set of MFM images, the lift height was kept the same, and the line scan time was 1.2 s. We used an R9 controller from RHK Technology with a built-in phase-locked loop. The resonant frequency of the cantilever was about 40 kHz. The tip was coated sequentially with 5-nm-thick Cr, 50-nm-thick Fe and 5-nm-thick Au films by electron beam deposition. The coated tip was magnetized perpendicular to the cantilever with a permanent magnet before it was loaded onto the scanning head. The coercivity of the magnetic coating was about 250 Oe and the saturation field was about 2,000 Oe. More details of the custom-designed MFM system can be found in a recent work[54].

Modelling of TKE on a Kondo lattice

To reveal the microscopic mechanism of TKE, we considered a Kondo lattice as formulated by equation (1). The evolution of localized spins is described by the Landau–Lifshitz–Gilbert (LLG) equation[38]:

$$\frac{\mathrm{d}\mathbf{n}_i}{\mathrm{d}t} = -\frac{\gamma}{(1+\alpha^2)\mu_i}\mathbf{n}_i \times \mathbf{B}_i^{\mathrm{eff}} - \frac{\gamma\alpha}{(1+\alpha^2)\mu_i}\mathbf{n}_i \times \left(\mathbf{n}_i \times \mathbf{B}_i^{\mathrm{eff}}\right). \quad (4)$$

Here the subscript i indexes the spin sites; the first and second terms on the right-hand side represent, respectively, the precession and damping of the normalized local spin $\mathbf{n}_i$, which is related to $\mathbf{m}_i$ in equation (1) of the main text by $\mathbf{m}_i = \mu_i \mathbf{n}_i$; $\gamma = 0.176$ rad T^{-1} ps^{-1} is the electron gyromagnetic ratio and α is the Gilbert damping parameter (set to 0.01 in our simulations). The local effective field $\mathbf{B}_i^{\mathrm{eff}} = -\partial H_{\mathrm{M}}/\partial \mathbf{n}_i$ originates from both the intrinsic exchange couplings and the external magnetic field. Equation (4) was numerically integrated by using the Depondt's modified Heun method[55] as implemented in the Spirit code[39]. The time step and temperature were set to $\delta t = 5$ fs and $T = 0.01$ K, respectively. The thermal effect was modelled by a stochastic field $\mathbf{B}_i^{\mathrm{th}}$ satisfying[56]

$$\mathbf{B}_i^{\mathrm{th}} = \sqrt{2\alpha k_{\mathrm{B}} T\mu_i/\gamma/\delta t} \times \boldsymbol{\eta}_i(t). \quad (5)$$

Here $\boldsymbol{\eta}_i(t)$ is the white noise for spin site i, which follows the normal random distribution and is updated for each time step; k_{B} is the Boltzmann constant.

We started from a random configuration under the out-of-plane applied external field B_z. The field B_z was progressively decreased from $B_{\max}$ to $-B_{\max}$ and then increased back to $B_{\max}$, with $B_{\max} = 0.116J$ sufficient to reach the magnetic saturation. At each field strength, the spin lattice was fully relaxed for 7,500 ps to reach equilibrium. Afterwards, we extracted the equilibrated snapshot configurations $\{\mathbf{m}_i(\mathbf{B})\}$ and inserted them into equation (1). Then we diagonalized the tight-binding Hamiltonian and calculated the optical conductivity by using the Kubo–Greenwood formula[48–50]:

$$\sigma_{\alpha\beta}(\hbar\omega) = \frac{\mathrm{i}e^2\hbar}{N_k\Omega_{\mathrm{c}}}\sum_{\mathbf{k},m,n}\frac{f_{m\mathbf{k}} - f_{n\mathbf{k}}}{\epsilon_{m\mathbf{k}} - \epsilon_{n\mathbf{k}}}\frac{\langle\psi_{n\mathbf{k}}|\hat{v}_\alpha|\psi_{m\mathbf{k}}\rangle\langle\psi_{m\mathbf{k}}|\hat{v}_\beta|\psi_{n\mathbf{k}}\rangle}{\epsilon_{m\mathbf{k}} - \epsilon_{n\mathbf{k}} - (\hbar\omega + \mathrm{i}\eta)}. \quad (6)$$

Here α and β are Cartesian directions, $\hat{v}_\alpha$ and $\hat{v}_\beta$ are the velocity operators, and Ω_{c} is the cell area. $\varepsilon_{m\mathbf{k}}$ and $\psi_{m\mathbf{k}}$ are the energy and wave function of the eigenstate with band index m and momentum $\mathbf{k}$, with the occupation $f_{m\mathbf{k}}$ determined by the Fermi–Dirac distribution (half filling is assumed). The constants e and $\hbar$ are the elementary charge and reduced Planck constant, respectively. The adjustable smearing parameter η is set to 0.1 eV for our calculations.

Data availability

Source data are provided with this paper. All other data that support the plots within this paper and other findings of this study are available from the corresponding author upon reasonable request.

Code availability

The Spirit code and manual are available at https://spirit-code.github.io/. Codes for reproducing the simulation results are available from the corresponding author upon reasonable request.

References

54. Zhang, Y. et al. Glovebox-assisted magnetic force microscope for studying air-sensitive samples in a cryogen-free magnet. *Rev. Sci. Instrum.* **95**, 013701 (2024).
55. Depondt, P. & Mertens, F. G. Spin dynamics simulations of two-dimensional clusters with Heisenberg and dipole–dipole interactions. *J. Phys. Condens. Matter* **21**, 336005 (2009).
56. Chubykalo, O., Hannay, J. D., Wongsam, M., Chantrell, R. W. & Gonzalez, J. M. Langevin dynamic simulation of spin waves in a micromagnetic model. *Phys. Rev. B* **65**, 184428 (2002).

Acknowledgements

We thank C. Gao, M. Tian, H. Du, J. Li, X. Yu, J. Wrachtrup, Q. Sun, Y. Zhang, Y. Wang, X. Wang and many other colleagues from their groups for various suggestions and efforts on potential direct detection of skyrmions in the newly synthesized magnet of $CrVI_6$. This work was supported by the National Natural Science Foundation of China (Grant Nos. 11574316, 11722435, 11804210, 11904350, 11974323, 12374458, U2032218, 12274276, 51627901 and U1932216), the Innovation Programme for Quantum Science and Technology (Grant No. 2021ZD0302800), the Strategic Priority Research Programme of Chinese Academy of Sciences (CAS) (Grant No. XDB0510200), the Anhui Initiative in Quantum Information Technologies (Grant No. AHY170000), the Anhui Provincial Natural Science Foundation (Grant. No. 2008085QA30) and National Synchrotron Radiation Laboratory (KY2060000177). C.L. and Z.S. gratefully acknowledge financial support from the National Key R&D Programme of China (Grant Nos. 2021YFA1600200, 2017YFA0303603 and 2023YFA1607701), the Plan for Major Provincial Science & Technology Project (Grant No. 202003a05020018), the Key Research Programme of Frontier Sciences, CAS (Grant No. QYZDB-SSW-SLH011), and the Users with Excellence Programme of Hefei Science Center, CAS (Grant No. 2021HSC-UE009). A portion of this work was performed on the Steady High Magnetic Field Facilities, High Magnetic Field Laboratory, CAS, and supported by the High Magnetic Field Laboratory of Anhui Province. This research was also partially carried out at the USTC Center for Micro and Nanoscale Research and Fabrication.

Author contributions

Z.Z. conceived the central idea and directed the project. H.Z., P.C., X.X. and Z.Z. predicted the $CrVI_6$ monolayer as a new 2D magnet. X.L. and S.Z. performed theoretical modelling and analysis. Ying Zhang synthesized the samples and fabricated the devices for MOKE measurements under supervision of B.X. F.H. and R.C. performed atomic-force-microscopy characterization of the thickness of $CrVI_6$ flakes. C.L. and De Hou performed MOKE measurements under supervision of Z.S. Yuchen Zhang and W.M. performed MFM imaging under supervision of Q.L. T.L., T.M., C.K., W.Z. and X.X. performed various syntheses and characterizations of CrI_3 and VI_3 crystals, devised methods for protection of the $CrVI_6$ samples at varying Cr/V ratios, and carried out subsequent electrical transport measurements. Dazhi Hou contributed to the conceptual development. All authors contributed to the interpretation of the data. X.L., S.Z. and Z.Z. wrote the paper with input from all the authors.

Competing interests

The authors declare no competing interests.

Additional information

Supplementary information The online version contains supplementary material available at https://doi.org/10.1038/s41567-024-02465-5.

Correspondence and requests for materials should be addressed to Zhigao Sheng, Bin Xiang or Zhenyu Zhang.

Peer review information *Nature Physics* thanks the anonymous reviewer(s) for their contribution to the peer review of this work.